GEOPHYSICS, VOL. 81, NO. 3 (MAY-JUNE 2016); P. KS123–KS134, 13 FIGS.
10.1190/GEO2015-0300.1

Microseismic event localization by acoustic time reversal extrapolation

Zhenhua Li[1] and Mirko van der Baan[1]

ABSTRACT

Traditional ray-based methods for microseismic event localization require picking of P- and S-wave first arrivals, which is often time consuming. Polarization analysis for each event is often also needed to determine its absolute location. Location methods based on reverse time extrapolation avoid the need for first-arrival time picking. Traditional reverse time extrapolation only incorporates particle velocity or displacement wavefields. This is an incomplete approximation of the acoustic representation theorem, which leads to artifacts in the back-propagation process. For instance, if the incomplete approximation is used for microseismic event locations using three-component (3C) borehole recordings, it produces a ghost event on the opposite side of the well, which leads to ambiguous interpretations. We have developed representation-theorem-based reverse time extrapolation for microseismic event localization, combining the 3C particle velocities (displacements) and the pressure wavefield. The unwanted ghost location is removed by explicitly incorporating a wavefield and its spatial derivative. Moreover, polarization analysis is not needed, because wavefields will focus at its absolute location during back propagation. Determination of microseismic event locations using wavefield extrapolation also necessitates a robust focusing criterion. The Hough transform allows for accurate determination of source timing and location by summing wavefront energy in the time-space domain. Synthetic examples demonstrated the good performance of the wavefield extrapolation scheme and focusing criterion in complex velocity fields for borehole acquisition geometries.

INTRODUCTION

Microseismic monitoring involves the acquisition of continuous seismic data for the purpose of locating and characterizing seismic activity induced by human activities, such as mining and hydraulic fracturing (van der Baan et al., 2013). In the mining industry, microseismicity is often acquired to monitor in situ stress changes around tunnel walls, preventing possible explosive rock failure (Maxwell, 2009). The most common application of this technology in the hydrocarbon industry is to monitor hydraulic fracturing treatments for increasing oil and gas production. During this process, high-pressure fluid is injected into a treatment well (Figure 1a). When the effective pressures overcome the rock strength, cracks are created in the formation, leading to microseismic emissions. Sensors are deployed in the borehole or on the surface (Figure 1a) to detect the resulting wave motion. Accurate microseismic event locations aid in understanding reservoir development, estimating simulated rock volumes, and determining future drainage strategies (Maxwell, 2009).

Generally, microseismic event localization methods are categorized into two types: (1) traveltime-based and (2) migration-based methods. The first method requires accurately picking P- and S-wave arrivals before further processing. However, event picking can often be a challenging and time-consuming task for low-quality data (Artman et al., 2010). The mispicks and missing picks negatively influence event locations (Kocon and van der Baan, 2012; Castellanos and van der Baan, 2013; Castellanos and van der Baan, 2015).

Migration-based methods avoid arrival time picking, possibly rendering them more suitable for low signal-to-noise ratio (S/N) data (Artman et al., 2010). In their simplest form, traveltime tables are created for each possible grid location. A semblance analysis over the forward predicted traveltimes then yields potential microseismic event locations (Duncan et al., 2008). In this method, a 3D grid volume is created in which each grid represents a possible microseismic event location. Then, time shifts that correspond to the traveltime from each possible location to all receivers are applied to the microseismic records followed by semblance analysis of the

Manuscript received by the Editor 5 June 2015; revised manuscript received 21 November 2015; published online 12 April 2016.
[1]University of Alberta Edmonton, Department of Physics, Edmonton, Alberta, Canada. E-mail: zhenhua3@ualberta.ca; mirko.vanderbaan@ualberta.ca.

time-shifted microseismic records. The grid point with the highest semblance energy can be considered as the most likely possible event location for a relatively accurate velocity model (Chambers and Kendall, 2008; Duncan et al., 2008).

In this paper, we explore time reversal extrapolation for determining microseismic event locations. This method is similar to reverse time migration (RTM) (Baysal et al., 1983; McMechan, 1983; Whitmore, 1983). In traditional RTM, the receiver-side particle displacement (or particle velocity) wavefield is injected into a smoothed velocity model, followed by application of an imaging condition. Sharp contracts in the model will generate artifacts due to secondary reflections, which are avoided by smoothing. RTM has been used for earthquake fault imaging (McMechan et al., 1985), thus showing promise for determining event hypocenters.

Traditional time reversal extrapolation uses a finite-difference operator for extrapolation (Artman et al., 2010; Fleury and Vasconcelos, 2013). In this paper, we introduce an alternative migration-based algorithm based on the acoustic representation theorem, allowing us to use either pressure data, 3C particle displacement or velocities, or pressure and displacement. This has the advantage that it incorporates a wavefield and its derivatives in the imaging (Vasconcelos, 2013), thereby reducing uncertainty by mitigating ghost focusing.

We also introduce a new focusing criterion based on the Hough transform (Yip et al., 1992) to better determine the origin time and the hypocenter of recorded microseismic events. The advantage of the Hough transform is that it conveniently assesses focusing continuously in the time-space domain during back propagation through spatiotemporal stacking, instead of only at a specific instant in time.

In the paper, we first derive the acoustic representation-theorem-based microseismic-event-localization algorithm and then we describe the new focusing criterion. Finally, we demonstrate performance with several examples, comparing estimated event locations and their origin time using individual (either pressure or particle velocity fields) and multiple wavefields (pressure and particle velocity fields).

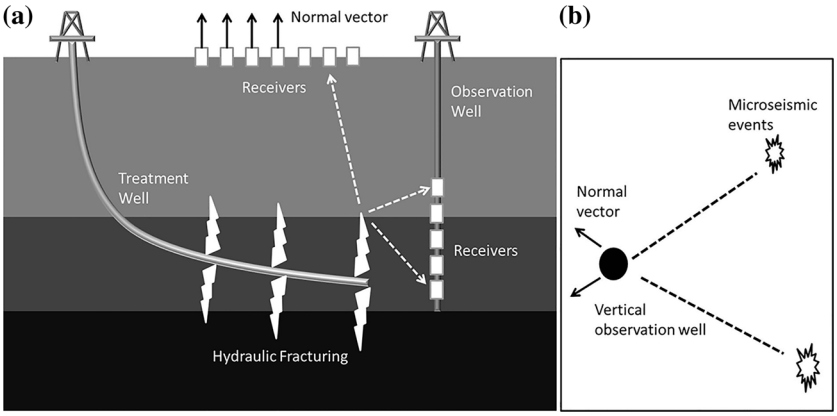

Figure 1. (a) Sideview of the hydraulic fracturing process. High-pressure fluid is injected through a treatment well, creating fractures in the surrounding rock. Emitted microseismic waves (dashed white lines) are recorded by receivers (white squares) on the surface or/and in the observation well. Observed waveforms are used to locate the microseismic events. The surface array has its normal vector pointing upward to the sky. (b) Map view of vertical observation geometry for microseismic event localization. Approximate angular range θ in normal vectors (solid black arrows) is determined by locations of perforation shots. Dashed black lines denote 2D planes defined by the vertical observation well and corresponding normal vectors.

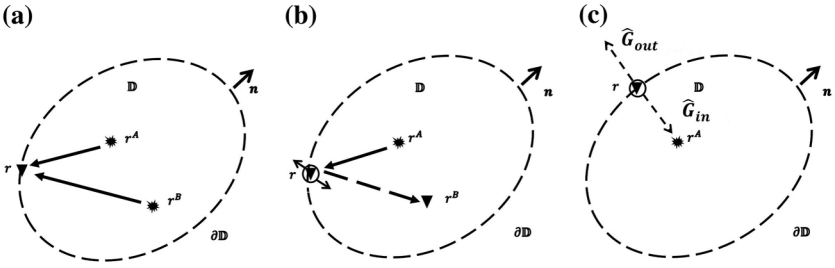

Figure 2. Illustration of the domains used for the (a) representation theorem and (b and c) back propagation. The enclosed domain consists of a volume $\mathbb{D}$ with boundary $\partial\mathbb{D}$. The vector n is the outward unit normal vector to the boundary $\partial\mathbb{D}$. (a) States A and B are wavefields generated by sources located at $\mathbf{r}^A$ and $\mathbf{r}^B$. The solid black arrows denote the wave path from source A or B (stars) to the receiver (triangle) located at $\mathbf{r}$ on the boundary. (b) $\mathbf{r}^A$: the microseismic event location and $\mathbf{r}^B$: an arbitrary location in back-propagation image. Solid black arrows: the wavepath from the microseismic event (star) to the receiver (triangle) located at $\mathbf{r}$ on the boundary. Dashed black arrow: the wavepath in the back propagation. Circle with two solid arrows: pressure wavefield and its gradient are recorded. (c) Circle with two dashed arrows: when either pressure or particle displacement/velocity wavefields are used, wavefields focusing at true event location $\mathbf{r}^A$ are $\hat{G}_{\text{ingoing}}$, whereas wavefields focusing at ghost location are $\hat{G}_{\text{outgoing}}$.

THEORY

The traditional RTM procedure involves back propagation of reflection data into the subsurface velocity model followed by an imaging condition (McMechan, 1983). For microseismic event localization, it is the same back-propagation procedure but with reflection data replaced by transmission data. In next section, we derive the general acoustic representation theorem for wavefield back propagation.

General acoustic representation theorem

Two independent states A and B are defined in the same 2D spatiotemporal domain $\mathbb{D} \subset \mathbb{R}$, with boundary $\partial\mathbb{D} \subset \mathbb{R}$ (Figure 2a). The normal vector pointing outward of $\partial\mathbb{D}$ is represented by n. States here simply mean a combination of material parameters, field quantities, source distributions, boundary conditions, and initial conditions that satisfy the relevant wave equation (van Manen et al., 2006). Though all our derivations are for the 2D case, they can be extended to 3D easily by adding a third dimension. Here, we assume that all other parameters in both states are the same except the sources. So, states A and B are expressed by the following first-order wave equations in the space-frequency domain:

state A/B:

$$\begin{cases} \nabla \hat{P}^{\mathrm{A/B}}(\mathbf{r},\omega) + \mathbf{i}\omega\rho(\mathbf{r})\hat{\mathbf{v}}^{\mathrm{A/B}}(\mathbf{r},\omega) = \hat{\mathbf{f}}^{\mathrm{A/B}}(\mathbf{r},\omega), \\ \nabla\cdot\hat{\mathbf{v}}^{\mathrm{A/B}}(\mathbf{r},\omega) + \mathbf{i}\omega\kappa(\mathbf{r})\hat{P}^{\mathrm{A/B}}(\mathbf{r},\omega) = \hat{q}^{\mathrm{A/B}}(\mathbf{r},\omega), \end{cases} \tag{1}$$

where A/B means equation 1 is valid for states A and B, ∇ is the spatial gradient operator, the hat $\hat{}$ indicates a frequency-domain variable, $\hat{P}^{\mathrm{A/B}}$ represents the pressure wavefield of state A/B, ρ is the medium density, κ is the medium compressibility, and $\hat{\mathbf{v}}^{\mathrm{A/B}}$ denotes the particle velocity of state A/B. The source of force $\hat{\mathbf{f}}^{\mathrm{A/B}}$ and the source of injection rate $q^{\mathrm{A/B}}$ are used for the sources of state A/B. Then, we apply the complex conjugate to state A of equation 1 to get a time reversed state A (Baysal et al., 1983; Fink, 1999; Wapenaar and Fokkema, 2006), yielding

$$\begin{cases} \nabla \hat{P}^{\mathrm{A}*}(\mathbf{r},\omega) - \mathbf{i}\omega\rho(\mathbf{r})\hat{\mathbf{v}}^{\mathrm{A}*}(\mathbf{r},\omega) = \hat{\mathbf{f}}^{\mathrm{A}*}(\mathbf{r},\omega), \\ \nabla\cdot\hat{\mathbf{v}}^{\mathrm{A}*}(\mathbf{r},\omega) - \mathbf{i}\omega\kappa(\mathbf{r})\hat{P}^{\mathrm{A}*}(\mathbf{r},\omega) = \hat{q}^{\mathrm{A}*}(\mathbf{r},\omega). \end{cases} \tag{2}$$

A correlation type of representation theorem is derived by calculating the surface integral of the interaction quantity $\nabla\cdot(P^{\mathrm{A}*}\mathbf{v}^{\mathrm{B}} + P^{\mathrm{B}}\mathbf{v}^{\mathrm{A}*})$ proposed by De Hoop (1988), whose expression in the frequency domain is given by

$$\begin{aligned} &\int_{\mathbb{D}} \nabla\cdot(\hat{P}^{\mathrm{A}*}\hat{\mathbf{v}}^{\mathrm{B}} + \hat{P}^{\mathrm{B}}\hat{\mathbf{v}}^{\mathrm{A}*})dS \\ &= \int_{\mathbb{D}} (\nabla\hat{P}^{\mathrm{A}*})\cdot\hat{\mathbf{v}}^{\mathrm{B}} + \hat{P}^{\mathrm{A}*}\nabla\cdot\hat{\mathbf{v}}^{\mathrm{B}} \\ &+ (\nabla\hat{P}^{\mathrm{B}})\cdot\hat{\mathbf{v}}^{\mathrm{A}*} + \hat{P}^{\mathrm{B}}\nabla\cdot\hat{\mathbf{v}}^{\mathrm{A}*}dS. \end{aligned} \tag{3}$$

For brevity, we omit the parameter dependence on frequency ω and spatial location $\mathbf{r}$. The surface integral on the left side of equation 3 can be expressed by a line integral around the enclosed area $\mathbb{D}$ using Stokes' theorem, producing

$$\begin{aligned} \oint_{\partial\mathbb{D}} \mathbf{n}\cdot(\hat{P}^{\mathrm{A}*}\hat{\mathbf{v}}^{\mathrm{B}} + \hat{P}^{\mathrm{B}}\hat{\mathbf{v}}^{\mathrm{A}*})dl = \int_{\mathbb{D}} (\nabla\hat{P}^{\mathrm{A}*})\cdot\hat{\mathbf{v}}^{\mathrm{B}} + \hat{P}^{\mathrm{A}*}\nabla \\ \cdot\hat{\mathbf{v}}^{\mathrm{B}} + (\nabla\hat{P}^{\mathrm{B}})\cdot\hat{\mathbf{v}}^{\mathrm{A}*} + \hat{P}^{\mathrm{B}}\nabla\cdot\hat{\mathbf{v}}^{\mathrm{A}*}dS, \end{aligned} \tag{4}$$

where $\mathbf{n}$ is the outward unit normal vector to the boundary. Combining equations 1 and 4, we get

$$\begin{aligned} \oint_{\partial\mathbb{D}} \mathbf{n}\cdot(\hat{P}^{\mathrm{A}*}\hat{\mathbf{v}}^{\mathrm{B}} + \hat{P}^{\mathrm{B}}\hat{\mathbf{v}}^{\mathrm{A}*})dl = \int_{\mathbb{D}} \hat{\mathbf{f}}^{\mathrm{A}*}\cdot\hat{\mathbf{v}}^{\mathrm{B}} + \hat{\mathbf{f}}^{\mathrm{B}} \\ \cdot\hat{\mathbf{v}}^{\mathrm{A}*} + \hat{q}^{\mathrm{B}}\hat{P}^{\mathrm{A}*} + \hat{q}^{\mathrm{A}*}\hat{P}^{\mathrm{B}}dS. \end{aligned} \tag{5}$$

Equation 5 is a general correlation type representation theorem without any boundary conditions and source assumptions. This type of representation is often used for wavefield backward extrapolation to get the characteristics of the seismic source (Aki and Richards, 2002).

In the above derivation, we link two independent wavefields by the general representation theorem without any assumptions on the source types. Next, we apply the correlation type representation theorem for time reversal extrapolation.

Time reversal extrapolation

First, we simplify the correlation type representation by considering assumptions on sources. We arbitrarily choose state A as the physical state that the recorded wavefield comes from an actual source at true location $\mathbf{r}^{\mathrm{A}}$, such as a microseismic event due to a hydraulic fracturing treatment. Then, we replace $\hat{P}^{\mathrm{A}*}$ with the more general form $\hat{P}^{*}(\mathbf{r},\mathbf{r}^{\mathrm{A}})$. Then, state B is the Green's state representing the wavefield from an impulsive explosive source at location $\mathbf{r}^{\mathrm{B}}$ inside the integral area.

We assume that a homogeneous medium exists outside of domain $\mathbb{D}$. The source $\hat{q}^{\mathrm{B}}$ is denoted by a Kronecker delta $\delta(\mathbf{r}-\mathbf{r}^{\mathrm{B}})$. The pressure wavefield corresponding to this source is the Green's function $\hat{G}(\mathbf{r},\mathbf{r}^{\mathrm{B}})$. State B is also called the Green's state. The particle velocity in both states can be written in the form of a pressure field, as $\hat{\mathbf{v}}^{\mathrm{A}*} = 1/(\mathbf{i}\omega\rho)\times[\nabla\hat{P}^{*}(\mathbf{r},\mathbf{r}^{\mathrm{A}})]$ and $\hat{\mathbf{v}}^{\mathrm{B}} = -1/(\mathbf{i}\omega\rho)\times[\nabla\hat{G}(\mathbf{r},\mathbf{r}^{\mathrm{B}})]$ (Curtis and Halliday, 2010). For simplicity, we assume that the volume source of force $\hat{\mathbf{f}}$ in both states equals zero (Wapenaar and Fokkema, 2006). Moreover, states A and B share the same medium properties within the boundary, giving a definition of states A and B,

state A:

$$\begin{cases} \nabla\hat{P}^{*}(\mathbf{r},\omega) = \mathbf{i}\omega\rho(\mathbf{r})\hat{\mathbf{v}}^{*}(\mathbf{r},\omega), \\ \nabla\cdot\hat{\mathbf{v}}^{*}(\mathbf{r},\omega) - \mathbf{i}\omega\kappa(\mathbf{r})\hat{P}^{*}(\mathbf{r},\omega) = \hat{s}^{*}(\omega)\hat{\delta}(\mathbf{r}-\mathbf{r}^{\mathrm{A}}), \end{cases} \tag{6}$$

state B:

$$\begin{cases} \nabla\hat{G}(\mathbf{r},\omega) = -\mathbf{i}\omega\rho(\mathbf{r})\hat{\mathbf{v}}_{G}(\mathbf{r},\omega), \\ \nabla\cdot\hat{\mathbf{v}}_{G}(\mathbf{r},\omega) + \mathbf{i}\omega\kappa(\mathbf{r})\hat{G}(\mathbf{r},\omega) = \hat{\delta}(\mathbf{r}-\mathbf{r}^{\mathrm{B}}), \end{cases} \tag{7}$$

where $\hat{s}^{*}(\omega)$ represents the source signature in the frequency domain and $\hat{\mathbf{v}}_{G}(\mathbf{r},\omega)$ represents the particle velocities corresponding to the Green's state B.

Under these assumptions, we get a further simplified correlation type representation theorem, given by

$$\begin{aligned} &\oint_{\mathbb{D}} \hat{P}^{*}(\mathbf{r},\mathbf{r}^{\mathrm{A}})\delta(\mathbf{r}-\mathbf{r}^{\mathrm{B}})\mathrm{dS} + \oint_{\mathbb{D}} \hat{s}^{*}(\omega)\hat{G}(\mathbf{r},\mathbf{r}^{\mathrm{B}})\hat{\delta}(\mathbf{r}-\mathbf{r}^{\mathrm{A}})dS \\ &= -\int_{\partial\mathbb{D}} \mathbf{n}\cdot\left(-\hat{G}(\mathbf{r},\mathbf{r}^{\mathrm{B}})\frac{1}{\mathbf{i}\omega\rho}\nabla\hat{P}^{*}(\mathbf{r},\mathbf{r}^{\mathrm{A}})\right. \\ &\left. + \hat{P}^{*}(\mathbf{r},\mathbf{r}^{\mathrm{A}})\frac{1}{\mathbf{i}\omega\rho}\nabla\hat{G}(\mathbf{r},\mathbf{r}^{\mathrm{B}})\right)dl, \end{aligned} \tag{8}$$

where the first part on the left side equals $\hat{P}^{*}(\mathbf{r}^{\mathrm{B}},\mathbf{r}^{\mathrm{A}})$ according to the delta function property and $\hat{G}(\mathbf{r},\mathbf{r}^{\mathrm{B}})$ is replaced with $\hat{G}(\mathbf{r}^{\mathrm{B}},\mathbf{r})$ through source-receiver reciprocity (Wapenaar and Fokkema, 2006).

The second term on the left side of equation 8 is called an acoustic sink. During time reversal, it ensures that a wavefield collapsed onto its source location disappears. Normally, it cannot be calculated directly, so the converged wavefield diverges again (Fink, 1999). Therefore, a focusing criterion is generally used, such as the Hough transform in the next section, to determine wavefield convergence onto the source location.

The left side of equation 8 can be written as $\hat{P}^*_{\mathrm{TR}} = \hat{P}^*(\mathbf{r}^{\mathrm{B}}, \mathbf{r}^{\mathrm{A}}) + \oint_{\mathbb{D}} \hat{s}^*(\omega)\hat{G}(\mathbf{r}^{\mathrm{B}}, \mathbf{r}^{\mathrm{A}})dS$ for simplicity, where $\hat{P}^*_{\mathrm{TR}}$ is the time reversed pressure wavefield without acoustic sink. Then, we get the time reversed extrapolation formula, given by

$$\hat{P}^*_{\mathrm{TR}}(\mathbf{r}^{\mathrm{B}}, \mathbf{r}^{\mathrm{A}}) = -\oint_{\partial\mathbb{D}} \mathbf{n}\cdot\left(-\hat{G}(\mathbf{r}^{\mathrm{B}}, \mathbf{r})\frac{1}{\mathbf{i}\omega\rho}\nabla\hat{P}^*(\mathbf{r}, \mathbf{r}^{\mathrm{A}}) + \hat{P}^*(\mathbf{r}, \mathbf{r}^{\mathrm{A}})\frac{1}{\mathbf{i}\omega\rho}\nabla\hat{G}(\mathbf{r}^{\mathrm{B}}, \mathbf{r})\right)dl. \quad (9)$$

Figure 2b illustrates the physical meaning of equation 9. A circle connected with arrows means the pressure wavefield $P(\mathbf{r}, \mathbf{r}^{\mathrm{A}})$ and its gradient $\nabla P(\mathbf{r}, \mathbf{r}^{\mathrm{A}})$ are recorded on the boundary $\partial\mathbb{D}$ from the microseismic event located at $\mathbf{r}^{\mathrm{A}}$. The two types of wavefields are back propagated separately using a given velocity profile. The pressure wavefield at arbitrary location $\mathbf{r}^{\mathrm{B}}$ within the boundary is calculated through combination of the back-propagated particle velocity $\hat{\mathbf{v}}^*(\mathbf{r}, \mathbf{r}^{\mathrm{A}}) = 1/(\mathbf{i}\omega\rho)\times[\nabla\hat{P}^*(\mathbf{r}, \mathbf{r}^{\mathrm{A}})]$ and pressure wavefield $\hat{P}^*(\mathbf{r}, \mathbf{r}^{\mathrm{A}})$. The location with the highest focus is considered as the most likely possible event location assuming a relatively correct velocity model.

Ghost focus cancellation

Traditional reverse time extrapolation only injects direct arrivals of particle displacement/velocity wavefields. Seismic waves focus not only at the true event location but also on a false location especially for limited borehole observation geometries. We call the false source location a ghost focus because it does not exist in reality.

In the following, we prove that representation-theorem-based reverse time extrapolation can remove the ghost focus as long as a correct normal vector n is chosen. We first write $\hat{G}(\mathbf{r}^{\mathrm{B}}, \mathbf{r}) = \hat{G}_{\mathrm{in}}(\mathbf{r}^{\mathrm{B}}, \mathbf{r}) + \hat{G}_{\mathrm{out}}(\mathbf{r}^{\mathrm{B}}, \mathbf{r})$, where the subscripts in and out refer to waves propagating toward true and false event's locations from the source at $\mathbf{r}$ on $\partial\mathbb{D}$ (Figure 2c) and then $\hat{P}^*(\mathbf{r}, \mathbf{r}^{\mathrm{A}})$ is written as $\hat{P}^*_{\mathrm{in}}(\mathbf{r}, \mathbf{r}^{\mathrm{A}})$, denoting that the seismic records come from true microseismic event. Equation 9 becomes

$$\begin{aligned}\hat{P}^*_{\mathrm{TR}}(\mathbf{r}^{\mathrm{B}}, \mathbf{r}^{\mathrm{A}}) &= -\oint_{\partial\mathbb{D}} \mathbf{n}\cdot\left((-\hat{G}_{\mathrm{in}}(\mathbf{r}^{\mathrm{B}}, \mathbf{r}) - \hat{G}_{\mathrm{out}}(\mathbf{r}^{\mathrm{B}}, \mathbf{r}))\frac{1}{\mathbf{i}\omega\rho}\nabla\hat{P}^*_{\mathrm{in}}(\mathbf{r}, \mathbf{r}^{\mathrm{A}})\right.\\ &\left. + \hat{P}^*_{\mathrm{in}}(\mathbf{r}, \mathbf{r}^{\mathrm{A}})\left(\frac{1}{\mathbf{i}\omega\rho}\nabla\hat{G}_{\mathrm{in}}(\mathbf{r}^{\mathrm{B}}, \mathbf{r}) + \frac{1}{\mathbf{i}\omega\rho}\nabla\hat{G}_{\mathrm{out}}(\mathbf{r}^{\mathrm{B}}, \mathbf{r})\right)\right)dl. \end{aligned} \quad (10)$$

We approximate the normal derivatives of the Green's function with their high-frequency approximations by replacing ∇ with $\mp\mathbf{i}k(\mathbf{r})\|\cos(\alpha(\mathbf{r}))\|$, where $k(\mathbf{r})$ is the local wavenumber at $\partial\mathbb{D}$ and $\alpha(\mathbf{r})$ is the angle between pertinent rays and the normal on $\partial\mathbb{D}$, assuming the medium is smooth in the vicinity around $\partial\mathbb{D}$ (Wapenaar and Fokkema, 2006). The ingoing waves propagating toward the true event location get a minus sign in the high-frequency approximation, whereas the outgoing waves propagating toward the false event location have a plus sign. Equation 10 then becomes

$$\begin{aligned}\hat{P}^*_{\mathrm{TR}}(\mathbf{r}^{\mathrm{B}}, \mathbf{r}^{\mathrm{A}}) &= -\oint_{\partial\mathbb{D}}(-\hat{G}_{\mathrm{in}}(\mathbf{r}^{\mathrm{B}}, \mathbf{r})\frac{\mathrm{k}(\mathbf{r})\|\cos(\alpha_{\mathrm{A}}(\mathbf{r}))\|}{\omega\rho}\hat{P}^*_{\mathrm{in}}(\mathbf{r}, \mathbf{r}^{\mathrm{A}})\\ &- \hat{G}_{\mathrm{out}}(\mathbf{r}^{\mathrm{B}}, \mathbf{r})\frac{k(\mathbf{r})\|\cos(\alpha_{\mathrm{A}}(\mathbf{r}))\|}{\omega\rho}\hat{P}^*_{\mathrm{in}}(\mathbf{r}, \mathbf{r}^{\mathrm{A}})\\ &- \hat{P}^*_{\mathrm{in}}(\mathbf{r}, \mathbf{r}^{\mathrm{A}})\frac{k(\mathbf{r})\|\cos(\alpha_{\mathrm{B}}(\mathbf{r}))\|}{\omega\rho}\hat{G}_{\mathrm{in}}(\mathbf{r}^{\mathrm{B}}, \mathbf{r})\\ &+ \hat{P}^*_{\mathrm{in}}(\mathbf{r}, \mathbf{r}^{\mathrm{A}})\frac{k(\mathbf{r})\|\cos(\alpha_{\mathrm{B}}(\mathbf{r}))\|}{\omega\rho}\hat{G}_{\mathrm{out}}(\mathbf{r}^{\mathrm{B}}, \mathbf{r}))dl, \end{aligned} \quad (11)$$

where angle $\alpha_{\mathrm{A}}(\mathbf{r})$ is for the true event at $\mathbf{r}^{\mathrm{A}}$ and angle $\alpha_{\mathrm{B}}(\mathbf{r})$ for an arbitrary location $\mathbf{r}^{\mathrm{B}}$. Stationary phase analysis shows that the contribution to the integral comes from those stationary points on $\partial\mathbb{D}$, at which the absolute cosines of $\alpha_{\mathrm{A}}(\mathbf{r})$ and $\alpha_{\mathrm{B}}(\mathbf{r})$ are identical (Schuster et al., 2004; Snieder, 2004; Wapenaar et al., 2004a; Snieder et al., 2006; Wapenaar and Fokkema, 2006). Besides, the signs of the first and the third terms are identical, but reversed for the second and forth terms. In other words, the back-propagated particle velocity and pressure fields have the same polarities when they are propagating toward the true location, but an opposite polarities in the directions of the ghost location. Thus, the second and forth terms of equation 10 cancel each other, leaving the first and third terms, meaning the waves only focus at the true event location when using the representation-theorem-based reverse time extrapolation, giving

$$\hat{P}^*_{\mathrm{TR}}(\mathbf{r}^{\mathrm{B}}, \mathbf{r}^{\mathrm{A}}) = -\oint_{\partial\mathbb{D}} \mathbf{n}\cdot\left(-\hat{G}_{\mathrm{in}}(\mathbf{r}^{\mathrm{B}}, \mathbf{r})\frac{1}{\mathbf{i}\omega\rho}\nabla\hat{P}^*_{\mathrm{in}}(\mathbf{r}, \mathbf{r}^{\mathrm{A}}) + \hat{P}^*_{\mathrm{in}}(\mathbf{r}, \mathbf{r}^{\mathrm{A}})\left(\frac{1}{\mathbf{i}\omega\rho}\nabla\hat{G}_{\mathrm{in}}(\mathbf{r}^{\mathrm{B}}, \mathbf{r})\right)\right)dl. \quad (12)$$

Implementation

For implementation, we use the discrete equivalent of equation 9 given by

$$\hat{P}^*_{\mathrm{TR}}(\mathbf{r}^{\mathrm{B}}, \mathbf{r}^{\mathrm{A}}) = -\sum_{\mathbf{r}}\mathbf{n}_{\mathbf{r}}\cdot\left(-\hat{G}(\mathbf{r}^{\mathrm{B}}, \mathbf{r})\frac{1}{\mathbf{i}\omega\rho}\nabla\hat{P}^*(\mathbf{r}, \mathbf{r}^{\mathrm{A}}) + \hat{P}^*(\mathbf{r}, \mathbf{r}^{\mathrm{A}})\frac{1}{\mathbf{i}\omega\rho}\nabla\hat{G}(\mathbf{r}^{\mathrm{B}}, \mathbf{r})\right), \quad (13)$$

where $\mathbf{n}_{\mathbf{r}}$ is the outward pointing normal of the integration boundary. The product in the first term on the right side represents the forward modeling process in the frequency domain. A wavefield $G(\mathbf{r}^{\mathrm{B}}, \mathbf{r})$ predicted at location $\mathbf{r}^{\mathrm{B}}$ by an explosive monopole source located at $\mathbf{r}$ is multiplied with the time reversed spatial gradient of the observed pressure wavefield denoted by $1/(\mathbf{i}\omega\rho)\times[\nabla\hat{P}^*(\mathbf{r}, \mathbf{r}^{\mathrm{A}})]$. The product in the second term on the right side also represents a forward modeling process in the frequency domain. $\nabla\hat{G}(\mathbf{r}^{\mathrm{B}}, \mathbf{r})$ represents the predicted wavefield at $\mathbf{r}^{\mathrm{B}}$ from a dipole source at location $\mathbf{r}$, convolved with the time reversed observed pressure wavefield $\hat{P}^*(\mathbf{r}, \mathbf{r}^{\mathrm{A}})$.

Figure 3 shows the processing flow of representation theorem-based time reversal extrapolation. For simplicity, we explain the problem under 2D implementation. Practical issues when extending to 3D will be introduced in a separate section. The pressure

wavefield and two components of the particle velocities are recorded. Before reverse time propagation, the data are first band-pass filtered to the range of interest. Then, the processed, complex conjugates of the pressure and 2C particle-velocity wavefields are multiplied with, respectively, the dipole and monopole Green's functions. This corresponds to convolution of the time reversed, observed wavefields with the appropriate Green's functions in the time domain. After both results are combined, a normal vector is used to control the contribution from each component (x and z). The choice of normal vector $\mathbf{n}_r$ depends on the predefined integration boundary.

In practice, we use the observed processed pressure wavefield at each receiver, reverse its time axis, and then forward propagate the resulting data into the medium using a finite-difference algorithm. Likewise, we back propagate the observed 2C velocity field. The final image is then obtained by stacking all corresponding wavefields for all receivers. This allows us to back propagate only the pressure or 2C wavefields individually but also stack their combined images. A focusing criterion, described next, is applied to the wavefield at each time slice to determine the origin time and hypocenter of the microseismic event.

Focusing criterion

A source focusing criterion is needed due to the absence of an acoustic sink in equations 9 and 13. In traditional reverse time imaging, the zero-lag crosscorrelation imaging condition determines focusing. But for microseismic event localization, we only have a receiver wavefield but no known source wavefield. The most straightforward focusing criteria use amplitude, energy, or semblance thresholding to determine possible event locations and origin times (Artman et al., 2010).

We use a modification of the Hough transform (Yip et al., 1992) to determine wavefield focusing. In essence, we assume that the wavefront is approximately circular around the source location point just before and after focusing and maximum energy concentration occurs at the origin time and location (Figure 4). Thus, as in Figure 4, if we sum the energy on the wavefront at time $t_0 - \Delta t$ and $t_0 + \Delta t$, as well as the energy at source location at time t_0, we should get a maximum value compared with the summation value at different locations and times. The modified Hough transform turns a back-propagated pressure wavefield image into a summation image in the spatiotemporal domain, from which we extract the source origin time and location. We name this summation image a Hough map. A back-propagated pressure wavefield image is called a wavefield map for comparison.

The first step is to do spatially circular summation. We sum the envelope of the back-propagated pressure wavefield P^*_{TR} along circles with local radius R around grid points $\mathbf{r}_x$ at time instance t_H, that is

$$P_H(\mathbf{r}_x, t_H) = \sum_{\mathbf{r}} \mathrm{Evn}(P^*_{\mathrm{TR}}(\mathbf{r}, t_H)), \tag{14}$$

where $\mathbf{r}$ satisfies $|\mathbf{r} - \mathbf{r}_x| = R$ and Evn represents the envelope of a time series. Grid points $\mathbf{r}_x$ generally represent a coarser grid than that used for the actual wave simulation. The time axis t_H is sampled every Δt seconds. Variable Δt is a prespecified time interval, such that the largest radii become approximately equal to half a dominant wavelength. Radius R is equal to local velocity $V(\mathbf{r}_x)$ times interval Δt. For small time intervals Δt, the actual wavefronts become circles with radii $\mathbf{r}$. This way, we turn the back-propagation image P^*_{TR} into a summation image P_H.

The next step is to do a temporal summation, which combines summed image P_H with back-propagation image P^*_{TR}, yielding a Hough map using

$$P^{\mathrm{sum}}_H(\mathbf{r}_x, t_H) = P_H(\mathbf{r}_x, t_H - \Delta t) + P_H(\mathbf{r}_x, t_H + \Delta t) + |(\mathrm{Evn}(P^*_{\mathrm{TR}}(\mathbf{r}_x, t_H)))|. \tag{15}$$

Hough map P^{sum}_H is evaluated for determining the most likely source location and origin time.

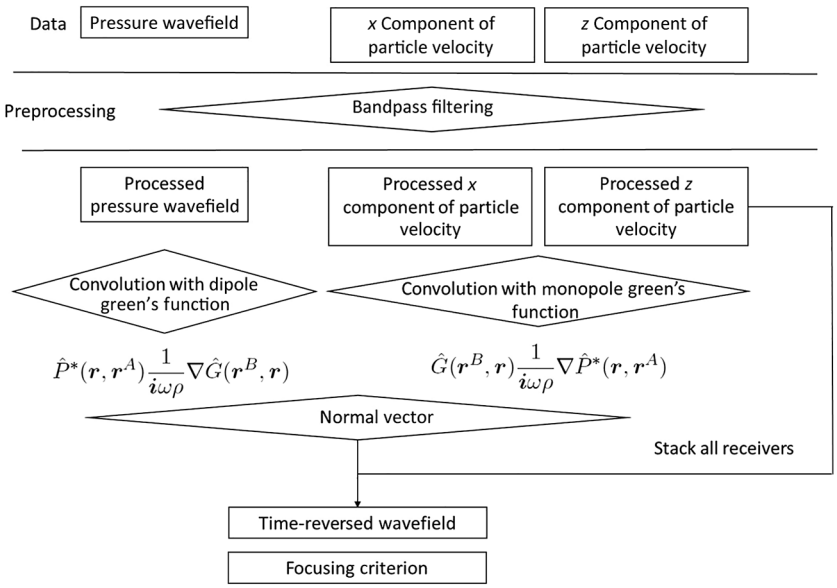

Figure 3. Processing flow of representation theorem-based time reversal extrapolation.

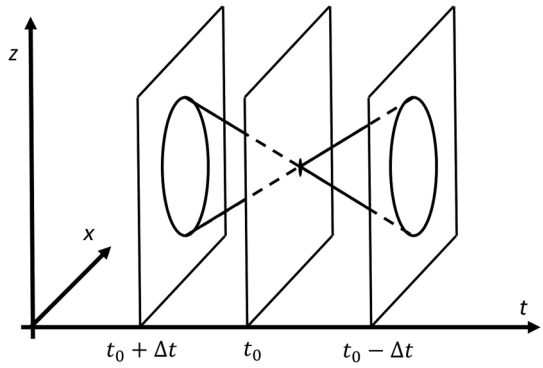

Figure 4. Wavefront in the back-propagation images. Z and X are the spatial coordinates and t is the back-propagation time. The black dot in the center time slice denotes source location, and t_0 is the source origin time. Circles: wavefront with radius $\mathbf{r}_{\delta t}$ right before and after origin time t_0. During back propagation, the wavefront collapses at the source location and then diverges again due to the lack of an acoustic sink.

We then assume that only a single microseismic event could occur at each time instant t_H. We save the spatial coordinates of the maximum value in the Hough map as a function of time t_H and compute its shortest distance to the receivers. This greatly condenses the information and allows us to select the most likely source locations and origin times without having to save either the Hough map or the back-propagation image at all time instances.

Next, a magnitude threshold $\mathbb{T}_M$ is set to determine the most likely source positions and origin times. A threshold $\mathbb{T}_D$ for the minimum distance to the receivers is also sometimes needed. In the back propagation, the highest magnitude of P_H^{sum} may appear at locations near the receivers due to uncancelled noise and signal interferences. These points thus generally represent artifacts and have to be excluded from the selection pool. Finally, the local maximum above the magnitude threshold in time and position is extracted to find the most likely source positions and origin times.

3D APPLICATION

Implementation of the representation theorem-based reverse time extrapolation becomes more complex in a 3D setting. Figure 1a shows two common observation systems for microseismic monitoring, namely, surface and borehole acquisitions. Each one has its own advantages and uncertainties when applying our proposed method.

Similar to conventional RTM, a large surface array has better coverage of microseismic events, producing located microseismic events with higher horizontal resolution. In this case, the normal vector is perpendicular to the 2D plane spanned by the receivers; in other words, it points upward (Figure 1a).

Borehole observations are more challenging for reverse time extrapolation. Normally, fewer than 20 geophones are used in a borehole scenario, leading to a very limited aperture. Also, no immediate choice of normal vector is available for this acquisition setup for a priori unknown event locations because an infinite amount of the 2D plane pass through a 1D borehole. Fortunately, we obtain a range of possible normal vectors from the borehole geometry and the locations of perforation shots (Figure 1b). First, the normal vectors are always perpendicular to the borehole. Only the azimuths of the normal vectors are to be determined. The range of azimuths can be further narrowed down by first locating several events for each hydraulic fracturing stage using ray-based methods, which provides a more appropriate range of azimuths before applying the representation-theorem-based reverse time extrapolation. The final choice of the azimuth of normal vector then ultimately varies with the actual acquisition geometry. If multiple boreholes exist, normals with back azimuths pointing to the centroid of the expected microseismic cloud will likely work well. Likewise, for strongly deviated wells, a normal perpendicular to the well with back azimuth pointing to the cloud's centroid should suffice. It is only in case of a single horizontal or vertical well that the choice of the optimal azimuth becomes truly challenging. These are the least optimal acquisition geometries for wavefield extrapolation-based event localization. One might have to take recourse to automated polarization analyses (De Meersman et al., 2006) for each event to estimate the azimuth of the required normal, with the possible advantage that only 2D planes are needed for wavefield extrapolation.

EXAMPLES

In this section, we apply the representation theorem-based reverse time extrapolation to synthetic examples using deviated borehole acquisitions as a challenging test situation. We use second order in time and fourth order in space finite differences to do forward modeling and back extrapolation. We smooth the velocity model during the back propagation to (1) mimic a partially unknown velocity field and (2) prevent the generation of reflections. We wish to explore the possibilities of this method in different velocity structures, namely, a layered model and the Marmousi velocity model. A homogeneous velocity example can be found in Li and van der Baan (2014).

Four-layer model

A deviated borehole is set in a four-layer velocity model with 43 receivers (Figure 5a), providing a good coverage of signal. The velocity of each layer can be found in Figure 5a. The source is an explosive source with a Ricker wavelet with a peak frequency of 60 Hz, located on the right of the well with coordinates (x and z) of (650 and 530 m). It simulates an event at origin time 0.02 s. The pressure and particle velocities in the horizontal and vertical directions are measured at each receiver, with a total recording time of 0.2 s. The numerical simulation grid spacing is 2.8 m with 0.18 ms time intervals. The synthetic, Gaussian white noise-contaminated data are shown in Figure 6.

Next, we inject three different combinations of the total wavefields using equation 13, namely, (1) using only the pressure data, (2) using both particle velocity fields but not pressure, and (3) using the pressure and velocity fields into a smoothed version of the exact velocity model (Figure 5b). The normal vectors are perpendicular to the well, pointing to the left side. Figure 7 displays the back-propagated source image for all three cases. Figure 7a is the case when we only back propagate the pressure data. Two high-energy images appear on both sides of the well at $t = 0.2$ s. The left location is a ghost focusing, whereas the right one is the true source location. Even though the energy of the ghost focus is slightly less than the true focus, it still brings ambiguity to the interpretation for the true location of the microseismic event. Figure 7b is the case when we only back propagate the 2C particle velocity data. The focusing features in this case are similar to the previous case, only the focuses have an opposite polarity from the previous case. When all data are back propagated, the energy of the ghost focus is significantly reduced. Only the true event location stands out clearly (Figure 7c). In addition, the combination of pressure and velocity fields for microseismic event localization leads to an improved S/N in the final image (Figure 7c), in particular around the receiver area, compared with the use of individual wavefields (Figure 7a and 7c).

We then test the ability of the focusing criterion for origin time and event location detection when pressure and velocity fields are used (combination 3). During back propagation, we apply equations 14 and 15 to the wavefield map P^*_{TR} to get the Hough map P_H at time t_H. The back-propagation grid spacing is 1.25 m, and the time interval for the focusing criterion is 2.8 ms. We then save the spatial coordinates of the maximum value in the Hough map P_H and the envelope of the wavefield P^*_{TR} as a function of time t_H and compute its shortest distance to the receivers before we apply threshold $\mathbb{T}_M$ and $\mathbb{T}_D$ (Figure 8). Maxima with distances less than 200 m are discarded (Figure 8a and 8c). The local

maximum in the Hough map occurs at 0.02 s at the true origin time (Figure 8b), whereas the maximum in the wavefield envelope happens at 0.03 s (Figure 8d). Moreover, the Hough criterion is better behaved in the sense that the variations are smoother and with a larger dynamic range, indicating that it is less sensitive to noise and imaging artifacts. Figure 9 displays the Hough map P_H and the envelope of the wavefield map P^*_{TR} at their respective detected origin times, showing that the Hough map is indeed more stable and accurate with fewer imaging artifacts.

Marmousi acoustic model

Next, we test the representation theorem-based reverse time extrapolation and focusing criterion under a more realistic situation

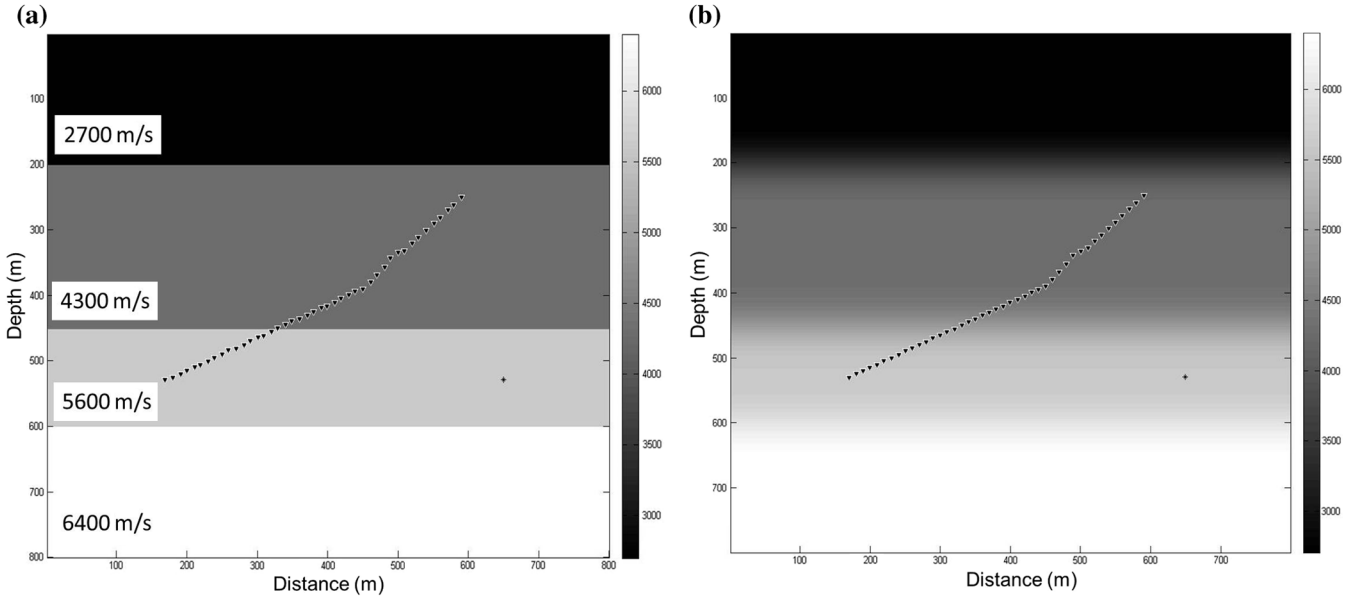

Figure 5. Two-dimensional acoustic layered velocity model. Red upside down triangles: receivers and blue cross: source. (a) True layered velocity model and (b) smoothed velocity model.

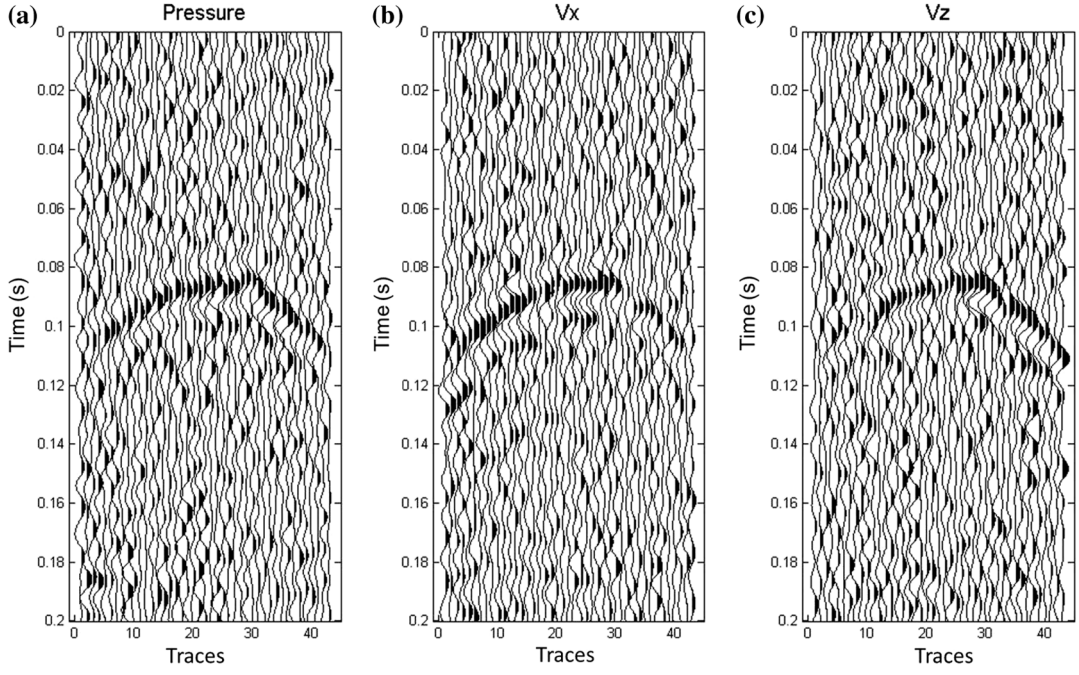

Figure 6. Seismic records for four-layer model including pressure and 2C particle velocity wavefields.

with a complex structure and a more complex source. In this example, the synthetic seismic records are created using the true Marmousi model (Figure 10a) with a double-couple (DC) source. The synthetic data from 14 borehole receivers are shown in Figure 11. A DC source with a Ricker wavelet with a dominant frequency of 10 Hz is located on the right of the well with coordinates (x and z) of (6500 and 2500 m). Its origin time is at 0.1 s. The simulation grid spacing is 24 m with 1.8 ms time interval.

We apply the focusing criterion in this example to a smoothed version of the exact velocity model (Figure 10b) for back propagation with the pressure and velocity fields (combination 3 in the previous example). The time interval for focusing criterion is 12.6 ms.

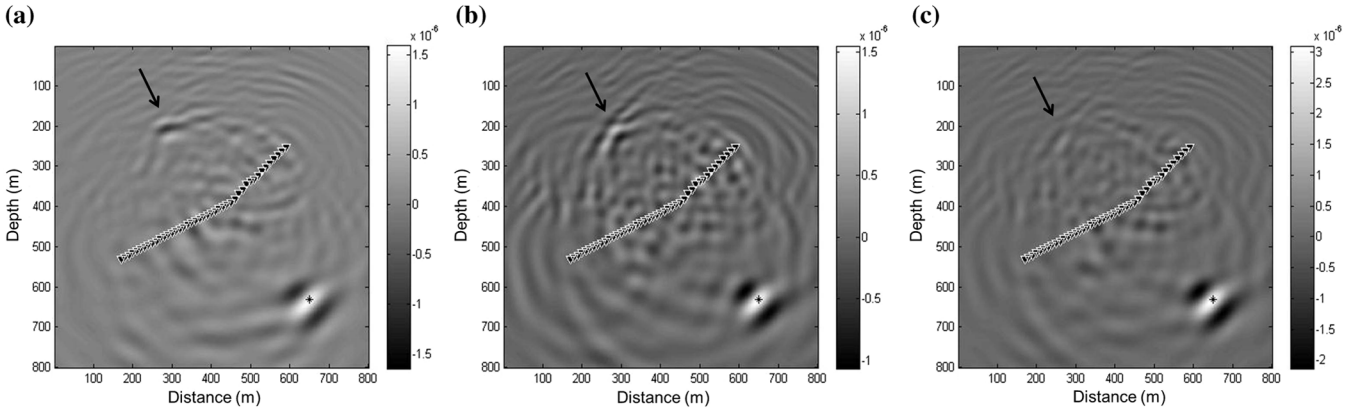

Figure 7. Comparison of the back-propagated pressure wavefield via three data combinations when using smoothed layered velocity model. (a) Pressure field only. (b) Particle velocity fields only. (c) Pressure field and particle velocity fields. The ghost location focusings (pointed by black arrows) exist in the first two cases. The ghost focusing is significantly suppressed in the third case when we combine all data.

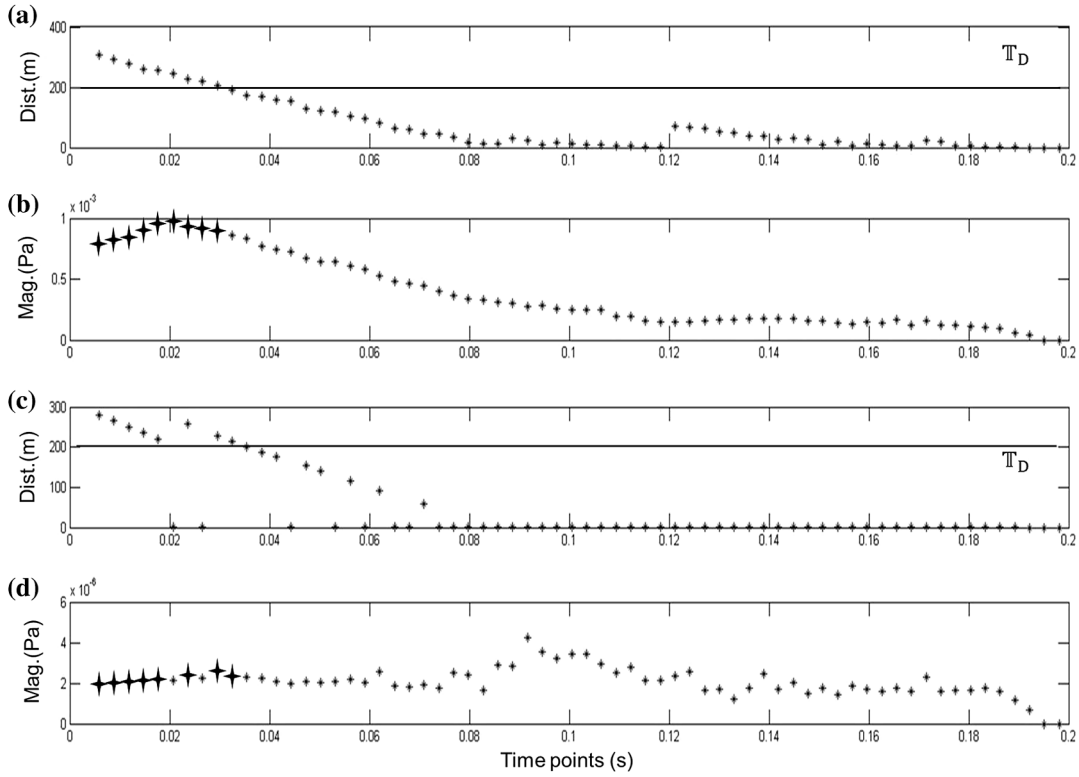

Figure 8. Event detection criteria using (a and b) maxima in Hough map or (c and d) maxima in wavefield envelopes for layered velocity model. (a and c) Distance of detected maximum to nearest receiver as a function of time. A minimum threshold $\mathbb{T}_D$ of 200 m is set (solid black line). All smaller distances are discarded. (b and d) Maximum value as a function of time. Black stars: maxima exceeding minimum distance. (b) Local Hough maximum is close to true origin time of 0.02 s and (d) contrary to maximum of wavefield envelope. (b) Extracted maxima from the Hough map also display smoother variations with a larger dynamic range than those from (d) the wavefield envelope.

Figures 12 displays the results for the focusing criteria using either the Hough map or the envelope of the wavefield in case of the smoothed velocity model, similar to Figure 8. For simplicity, we only show the magnitude points with reasonable distance to receivers. The Hough criterion predicts an origin time of 0.1 s and the envelope maximum occurs at 0.22 s. The appearance of noise introduces large errors to the origin time determined by the envelope of the wavefield (Figure 12b), whereas an accurate origin time is provided when using the Hough map-based focusing criterion (Figure 12a). Figure 13 shows the comparison of back-propagation images for corresponding origin times derived from the Hough criterion (Figure 13a) and the envelope maximum (Figure 13b). The

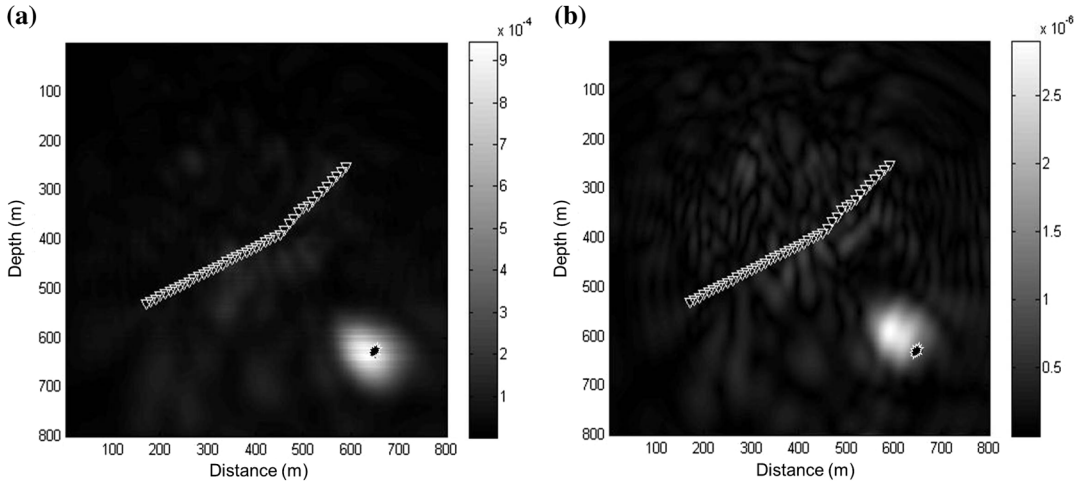

Figure 9. Comparison of the Hough map and envelope of the wavefield at respective estimated origin times for the layered velocity model. (a) Hough map at 0.02 s and (b) wavefield envelope at 0.03 s. Black star: true event location.

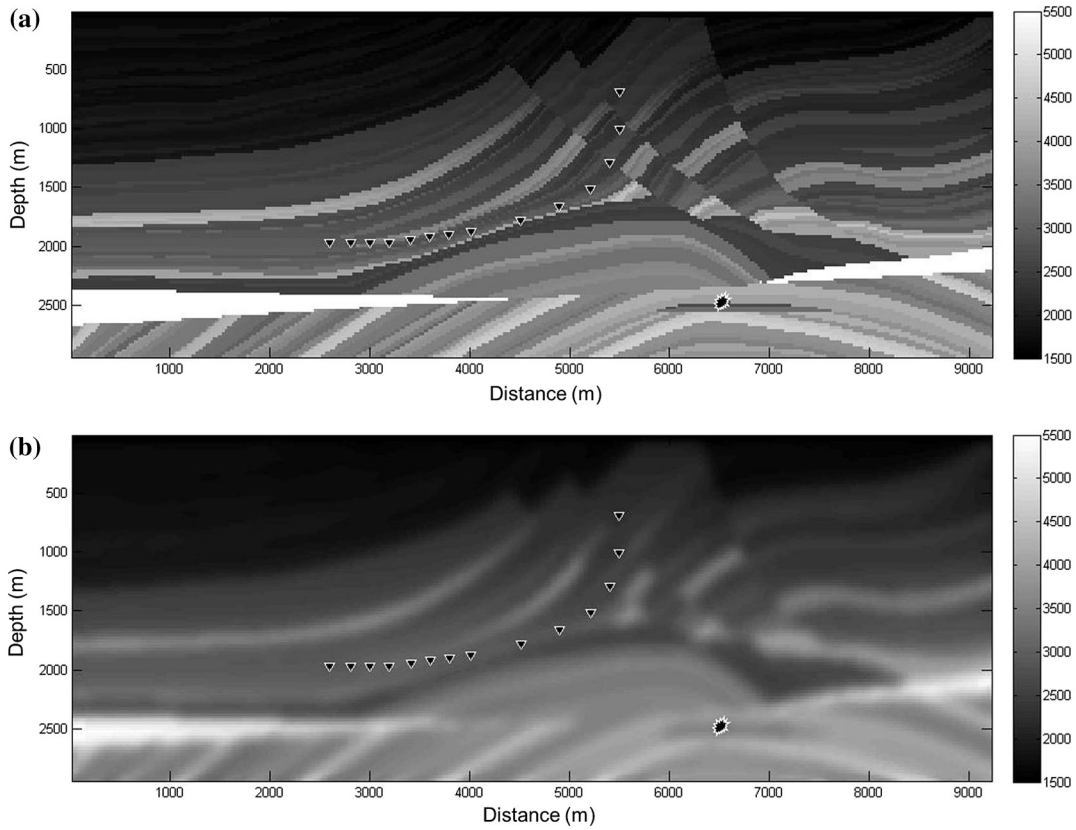

Figure 10. Two-dimensional acoustic Marmousi velocity model. Red upside down triangles: receivers and red star: source. From upper to bottom: (a) actual velocity model and (b) smoothed velocity model. Velocities are in m/s.

envelope maximum fails to locate the source properly because the radiation pattern of the DC source makes the magnitude of focus equal to zero. On the contrary, the Hough map leads to a more accurate event location, with less imaging artifacts.

DISCUSSION

In this paper, we have shown the advantages of combining the pressure and 3C particle displacement/velocity wavefields in microseismic event localization. Therefore, we advocate the combined use of hydrophone and 3C receivers in microseismic monitoring. The spatial derivatives of the pressure wavefield contain directional information that can aid in the back-propagation process. Acoustic representation theorem-based reverse time extrapolation naturally uses the two types of data. Moreover, all wavefields are back propagated to the source location independently and combined in the final step. The two types of wavefields generate an opposite-polarity image at the ghost location and the same-polarity image at the true event location. By adding the two wavefields, the opposite-polarization portions cancel each other, whereas the energy at the true location is boosted. This suppresses image artifacts compared with implementations when only the pressure wavefield or the spatial gradients are used. Moreover, the particle velocity and pressure records may have different S/Ns, e.g., due to contamination with different types of noise or different bandwidth sensitivities. Judicious weighting may thus enhance the final imaging quality of the reconstructed combined wavefields, as well as the Hough images, even further compared with the images from the individual wavefields. The combined use of pressure and particle velocity wavefields may equally improve migration of reflection seismic data (Vasconcelos, 2013).

The back-propagated wavefield does not collapse to a point in our tests due to the limited acquisition aperture but leaves an area with high energy concentration. This area provides the uncertainty in event location. A visual comparison for homogeneous and complex velocity models shows that the anticipated uncertainty in event locations using the proposed method is similar to those from traveltime-based methods as obtained using the sensitivity analysis of Feroz and van der Baan (2013). Location uncertainties may also result from velocity model error. The back-propagated wavefield may focus to a misplaced location under an incorrect velocity model. In particular, systematic biases from the true model may be problematic. However, use of a much more strongly smoothed velocity model than shown in Figure 10b still leads to acceptable locations. In case of erroneous velocities, the proposed Hough transform-based focusing criterion can still find the most focused points, but possibly at an incorrect location. Location uncertainties can be decreased with a more accurate velocity model and/or larger acquisition apertures. To increase the acquisition aperture, a combination of borehole and surface receivers may work

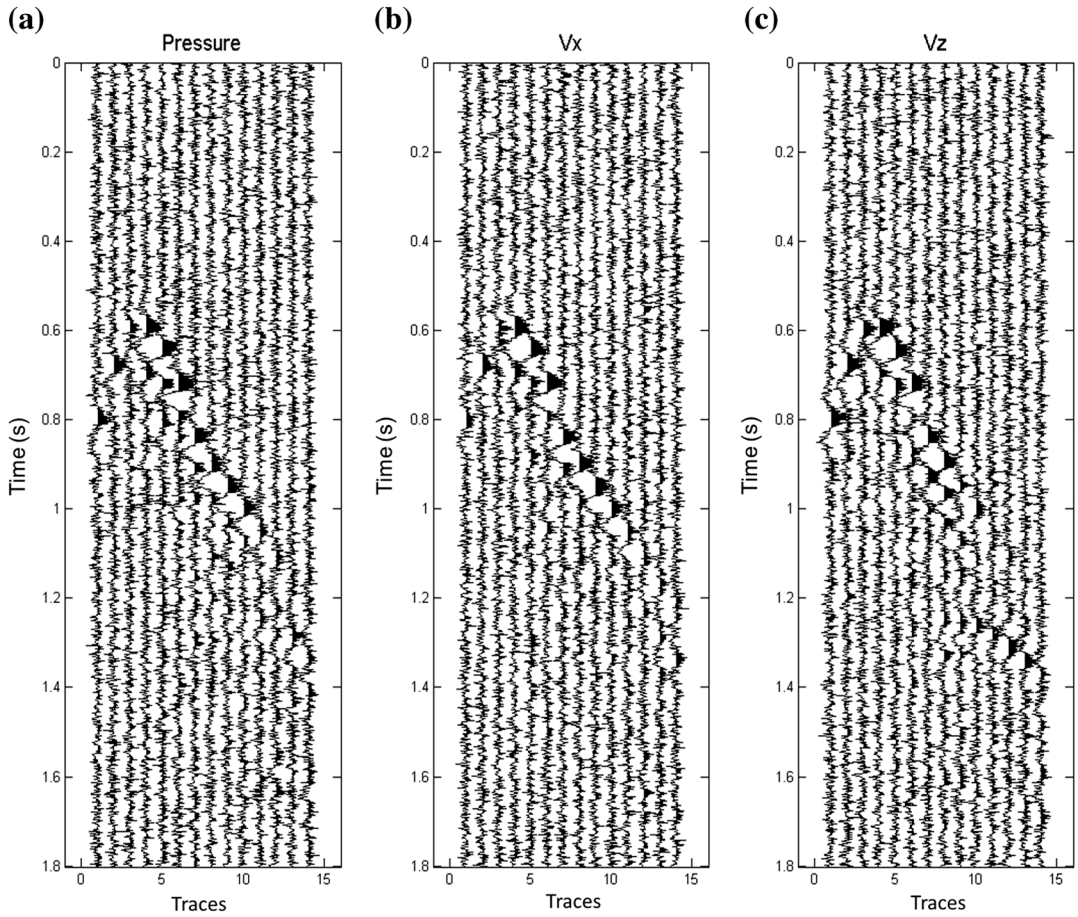

Figure 11. Synthetic noisy seismograms for Marmousi test model. The complex waveforms are due to the complex velocity structure. (a) Pressure field records. (b and c) x- and z-components of particle velocity fields records.

best. Indeed, even though our example includes purely borehole acquisitions, the methodology is readily applicable to surface recordings.

In the representation theorem, a normal vector to the boundary of the enclosed volume is needed in the calculation. That means the normal vector $n_{\mathbf{r}}$ should be specified prior to combination of the

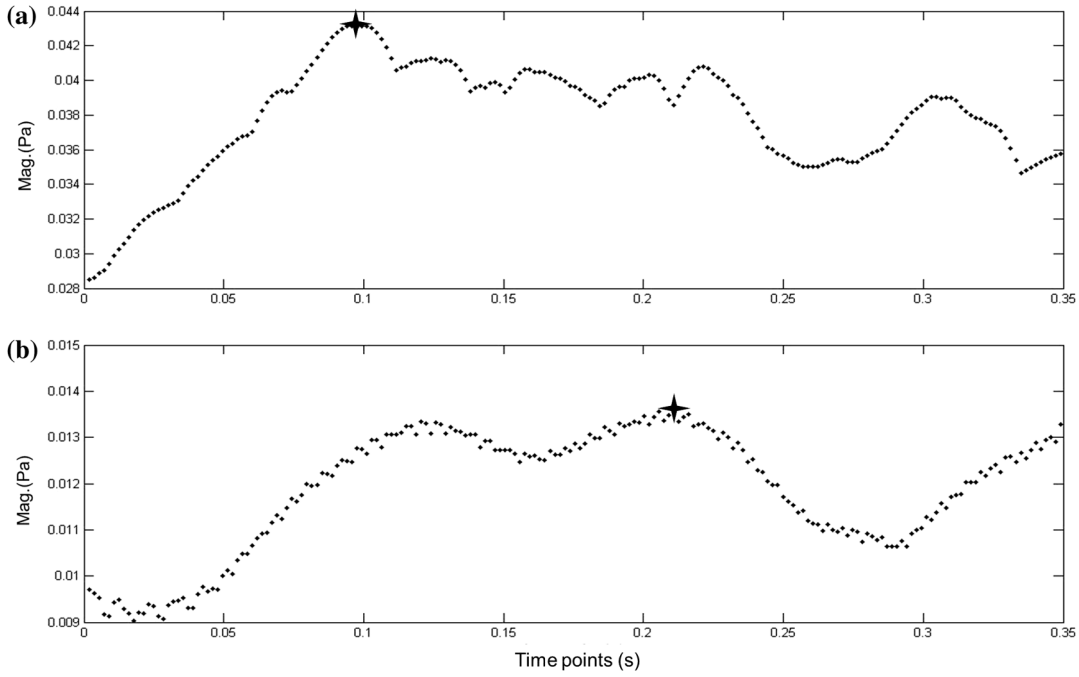

Figure 12. Zoom in from time 0 to 0.35 s for event detection criteria using (a) maxima in Hough map or (b) maxima in wavefield envelopes for smoothed Marmousi velocity model. See Figure 7 for labels. Detected origin times are respectively (a) 0.1 s (Hough map) and (b) 0.22 s (wavefield envelope). True origin time is at 0.1 s.

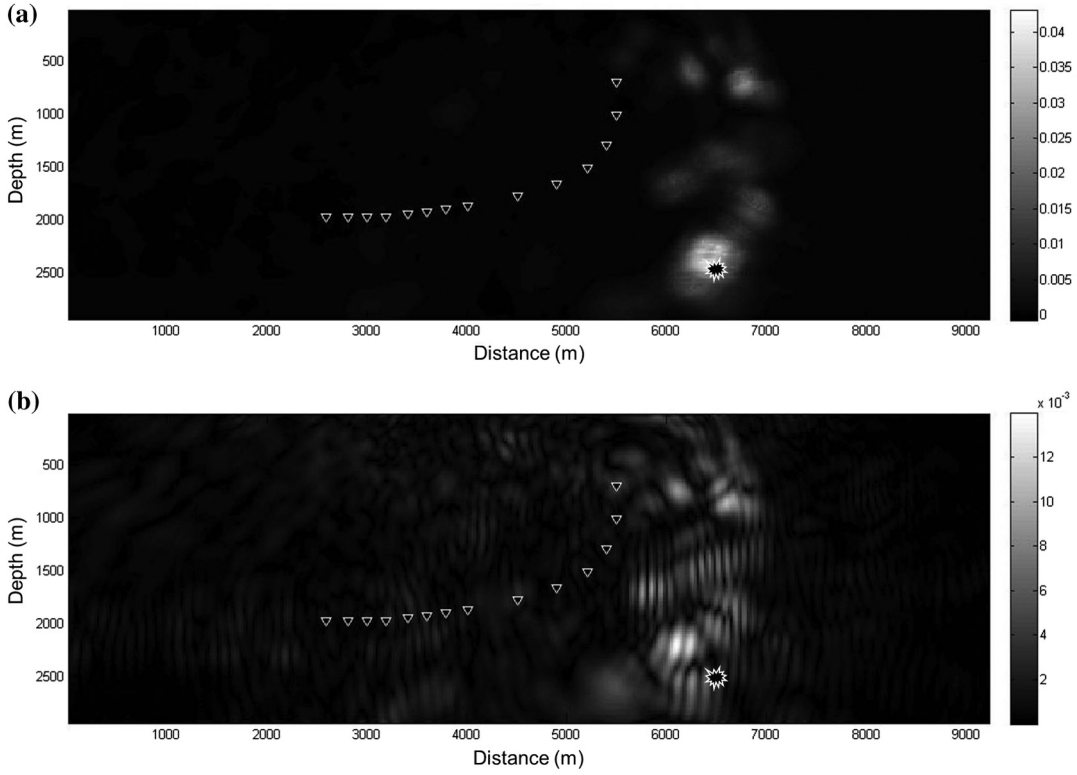

Figure 13. Comparison of the Hough map and envelope of the wavefield at respective estimated origin times for the smooth Marmousi velocity model. (a) Hough map at 0.1 s and (b) wavefield envelope at 0.22 s. Black star: true event location.

various wavefields. This leads to various possible choices especially if the receivers are located in a single borehole. For traditional surface land acquisition system, the normal vector is generally set as pointing upward, but for a straight well trajectory, the azimuth of the normal vector is not easily determined. So, we suggest approximating the normal vector according to the spatial relationship between observation and treatment wells. The property of ghost focusing cancellation can also help to determine the azimuth of microseismic events by finding the optimal focusing for different normal vectors. This is mainly because at the correct azimuth, the back-propagated pressure and particle velocity field should optimally align at one side of the borehole and fully cancel at the opposite side.

The performance of the modified Hough transform depends significantly on the ratio between acquisition aperture and source-receiver distance. The ratio has to be sufficiently large for successful focusing. A small ratio makes the back-propagated receiver-side wavefield diverge rather than converge where the assumption of circular wavefronts breaks down. Moreover, the distance from treatment well to observation well determines the $\mathbb{T}_D$ threshold. The microseismic events must exist beyond a reasonable range around the treatment well. High focusings inside of this range are not considered. The selection of the $\mathbb{T}_M$ threshold comprises a trade-off between the risk of detecting false events and missing true events. A high threshold lowers the risk of identifying false events but also increases the chance of missing true events. On the contrary, a low threshold increases the number of detected events but also the number of false alarms.

Finally, the computational time of the focusing criterion varies with respect to discrete time interval Δt_N. The computational time of the back-propagation process T_{bp} is proportional to $N_T N_X^d$, where N_T is the number of time steps and N_X is the number of grid points in dimension d (van Manen et al., 2006). For simplicity, we omit the number of flops needed for calculation of the discrete derivatives. The computational time for the focusing criterion T_{fc} is proportional to $N_T/\Delta t_N N_X^d$ because we only calculate a Hough image for every Δt_N time points. The additional computational time of the focusing criterion is different with different Δt_N, but generally it is smaller than 10% of the back-propagation time.

CONCLUSION

Representation theorem-based time-reversal extrapolation offers much promise for obtaining microseismic event locations without the need to first pick individual arrivals, in particular, if the pressure wavefield and its spatial gradients are available. The latter may require the combined usage of hydrophones and 3C particle-velocity sensors during microseismic acquisition to get improved microseismic event locations. The Hough map provides a convenient and stable criterion for automatically detecting event locations and origin times.

ACKNOWLEDGMENTS

We thank the sponsors of the Microseismic Industry Consortium for financial support and I. Vasconcelos for discussions. We also thank J. Shragge, J. van der Neut, B. Artman, and two anonymous reviewers for their constructive comments.

REFERENCES

Aki, K., and P. G. Richards, 2002, Quantitative seismology, 2 nd ed.: University Science Books.

Artman, B., I. Podladtchikov, and B. Witten, 2010, Source location using time-reverse imaging: Geophysical Prospecting, **58**, 861–873, doi: 10.1111/j.1365-2478.2010.00911.x.

Baysal, E., D. D. Kosloff, and J. W. C. Sherwood, 1983, Reverse time migration: Geophysics, **48**, 1514–1524, doi: 10.1190/1.1441434.

Castellanos, F., and M. van der Baan, 2013, Microseismic event locations using the double-difference algorithm: CSEG Recorder, **38**, 26–37.

Castellanos, F., and M. van der Baan, 2015, Waveform similarity for quality control of event locations, time picking and moment tensor solutions: Geophysics, **80**, no. 6, WC99–WC106, doi: 10.1190/geo2015-0043.1.

Chambers, K., and J.-M. Kendall, 2008, A practical implementation of wavefront construction for 3D isotropic media: Geophysical Prospecting, **58**, 821–830, doi: 10.1111/j.1365-2478.2010.00893.x.

Curtis, A., and D. Halliday, 2010, Source-receiver wave field interferometry: Physical Review E, **81**, 046601-1–046601-10, doi: 10.1103/PhysRevE.81.046601.

De Hoop, A. T., 1988, Time-domain reciprocity theorems for acoustic wave fields in fluids with relaxation: The Journal of the Acoustical Society of America, **84**, 1877–1882, doi: 10.1121/1.397152.

De Meersman, K., M. van der Baan, and J.-M. Kendall, 2006, Signal extraction and automated polarization analysis of multi-component array data: Bulletin of the Seismological Society of America, **96**, 2415–2430, doi: 10.1785/0120050235.

Duncan, P. M., J. D. Lakings, and R. A. Flores, 2008, Method for passive seismic emission tomography: U. S. Patent Application Publication US2008/0068928A1.

Feroz, A., and M. van der Baan, 2013, Uncertainties in microseismic event locations for horizontal, vertical and deviated boreholes: 83rd Annual International Meeting, SEG, Expanded Abstracts, 592–596.

Fink, M., 1999, Time-reversed acoustics: Scientific American, 91–97.

Fleury, C., and I. Vasconcelos, 2013, Adjoint-state reverse time migration of 4C data: Finite-frequency map migration for marine seismic imaging: Geophysics, **78**, no. 2, WA159–WA172, doi: 10.1190/geo2012-0306.1.

Kocon, K., and M. van der Baan, 2012, Quality assessment of microseismic event locations and traveltime picks using a multiplet analysis: The Leading Edge, **31**, 1330–1337, doi: 10.1190/tle31111330.1.

Li, Z. H., and M. van der Baan, 2014, Acoustic representation theorem based time-reversal-extrapolation for microseismic event localization: 84th Annual International Meeting, SEG, Expanded Abstracts, 2240–2244.

Maxwell, S., 2009, Assessing the impact of microseismic location uncertainties on interpreted fracture geometries: Presented at the 2009 SPE Annual Technical Conference and Exhibition.

McMechan, G. A., 1983, Migration by extrapolation of time-dependent boundary values: Geophysical Prospecting, **31**, 413–420, doi: 10.1111/j.1365-2478.1983.tb01060.x.

McMechan, G. A., J. H. Luetgert, and W. D. Mooney, 1985, Imaging of earthquake sources in Long Valley Valdera, California, 1983: Bulletin of the Seismological Society of America, **75**, 1005–1020.

Schuster, G. T., J. Yu, J. Sheng, and J. Rickett, 2004, Interferometric/daylight seismic imaging: Geophysical Journal International, **157**, 838–852, doi: 10.1111/j.1365-246X.2004.02251.x.

Snieder, R., 2004, Extracting the Green's function from the correlation of coda waves: A derivation based on stationary phase: Physics Review E, **69**, 046610-1–046610-8.

Snieder, R., K. Wapenaar, and K. Larner, 2006, Spurious multiples in seismic interferometry of primaries: Geophysics, **71**, no. 4, SI111–SI124, doi: 10.1190/1.2211507.

Van der Baan, M., D. Eaton, and M. Dusseault, 2013, Microseismic monitoring developments in hydraulic fracture stimulation, *in* A. P. Bunger, J. McLennan, and R. Jeffrey, eds., Effective and sustainable hydraulic fracturing: Intech, 439–466.

Van Manen, D.-J., A. Curtis, and J. O. A. Robertsson, 2006, Interferometric modeling of wave propagation in inhomogeneous elastic media using time reversal and reciprocity: Geophysics, **71**, no. 4, SI47–SI60, doi: 10.1190/1.2213218.

Vasconcelos, I., 2013, Source-receiver, reverse-time imaging of dual-source, vector-acoustic seismic data: Geophysics, **78**, no. 2, WA123–WA145, doi: 10.1190/geo2012-0300.1.

Wapenaar, K., and J. Fokkema, 2006, Green's function representations for seismic interferometry: Geophysics, **71**, no. 4, S133–S146, doi: 10.1190/1.2213955.

Wapenaar, K., D. Draganov, J. van der Neut, and J. Thorbecke, 2004a, Seismic interferometry: A comparison of approaches: 74th Annual International Meeting, SEG, Expanded Abstracts, 2269–2272.

Whitmore, D. N., 1983, Iterative depth imaging by back time propagation: 53th Annual International Meeting, SEG, Expanded Abstracts, 382–385.

Yip, R. K. K., P. K. S. Tam, and D. N. K. Leung, 1992, Modification of Hough Transform for circles and ellipses detection using a 2-dimensional array: Pattern recognition, **25**, 1007–1022, doi: 10.1016/0031-3203(92)90064-P.